

CS-TRD: a Cross Sections Tree Ring Detection Method

Henry Marichal¹, Diego Passarella,² Gregory Randall¹

¹ Instituto de Ingeniería Eléctrica, Facultad de Ingeniería, Universidad de la República,
 Uruguay(henry.marichal@fing.edu.uy / randall1@fing.edu.uy)

² Sede Tacuarembó, CENUR Noreste, Universidad de la República, Uruguay(diego.passarella@cut.edu.uy)

PREPRINT August 15, 2024

Abstract

This work describes a Tree Ring Detection method for complete Cross-Sections of Trees (CS-TRD) that detects, processes, and connects edges corresponding to the tree's growth rings. The method depends on the parameters for the Canny Devernay edge detector (σ), a resize factor, the number of rays, and the pith location. The first five are fixed by default. The pith location can be marked manually or using an automatic pith detection algorithm. Besides the pith localization, CS-TRD is fully automated and achieves an F-Score of 89% in the UruDendro dataset (of *Pinus taeda*) and of 97% in the Kennel dataset (of *Abies alba*) without specialized hardware requirements.

Source Code

A Python 3.11 implementation of CS-TRD is available on the web page of this article¹. Usage instructions are included in the `README.md` file of the archive. The associated online demo is accessible through the website.

Keywords: image edge detection, dendrochronology, tree ring detection

1 Introduction

Most of the available methods for dendrochronology (measurement and dating of tree growth rings) use images taken from cores (small cylinders crossing all the tree growth rings) instead of complete transverse cross sections. Figure 1 illustrates that core images are rectangular sections. Using cores for the analysis presents some advantages. The rings are measured on a small portion of the trunk, which can be assumed as a sequence of bands with repetitive contrast, simplifying the image analysis. However, this method provides limited information on annual tree growth because it results in a circular approximation based on a rectangular section. In many cases, ring growth is not uniform, leading to significant errors. An application that needs the study of the whole cross-section is when

¹<https://ipolcore.ipol.im/demo/clientApp/demo.html?id=77777000390>



Figure 1: Examples of core tree-ring images taken from a dataset with 239 images [6].

studying the angular homogeneity of the ring-tree pattern trying to detect the so-called compression wood [4] for which the lack of homogeneity in the growing pattern produces differential mechanical properties. On the downside, cross-section analysis implies the felling of the tree and includes the challenge of generating a pattern of (almost) concentric closed curves representing the tree rings. As Figure 2 shows, several factors increase the difficulty of the task: wood knots, fungi appearing as black spots with shapes following radial directions, and cracks that can be very wide.

This article presents a founded method for automatically delineating tree rings on cross-section RGB images. The approach takes advantage of the knowledge of the tree cross-section's general structure and redundant information on a radial profile for different angles around the tree's pith.

The method is evaluated over two public datasets with two different species and outperforms the other publicly available comparable method [7] in accuracy.

Section 2 briefly review previous work in the field. Section 3 describes the proposed automatic cross-section tree-ring detection algorithm (CS-TRD). Section 4 presents in more detail the algorithms and Section 5 discuss implementation details. Section 6 briefly presents a dataset for developing and testing the proposed approach and discusses some experimental results. Section 7 concludes and propose future work.

2 Previous work

Tree ring detection is an old and essential problem in forestry, and it has multiple uses in dendroecology, dendrochronology, forest management, and other applications. Due to the species idiosyncrasies, many practitioners still use a manual approach, using a ruler or other (manual) tree-ring measuring system, which is a tedious and time-consuming task that requires an expert operator.

Among the strategies proposed in recent years for the automation of tree ring delineation over wood cross-section images, we can mention the classic image-processing approaches that try to detect borders and then reconstruct the ring pattern [1, 14, 18, 9, 10, 11] and the algorithms based on deep learning methods which try to learn the solution from the data [7]. The core approaches are more extended, resulting in a significantly greater number of data sets. Hence, the deep learning methods are generally designed for core dendrochronology [5, 15].

Cerda et al. [1] proposed a classic image processing approach for detecting entire growth rings based on the Generalized Hough Transform. This work already suggests using the general geometrical structure of the tree rings, which we use in our approach, as illustrated in Figure 4. Norell et al. use the Grey Weighted Polar Distance Transform [14] to process end faces acquired in sawmill environments. Still, the method implies using rectangular sections, including the pith, and avoiding knots or other disturbances, diminishing the generality of the approach. Zhou proposes a much simpler method [18], which resembles the traditional manual procedure in which two perpendicular lines across the slice are traced. The watershed method is applied to the profiles to obtain the peaks corresponding to each ring. Henkel et al. use an active contours approach [9] alone or coupled with a Dual-Tree Complex Wavelet Transform [10] based on the evolution of a partial differential equation that includes terms related to the image content and to the curve itself. Many PDE-based algorithms are time-consuming, making them difficult to use in real-time applications. Makela et al. proposed

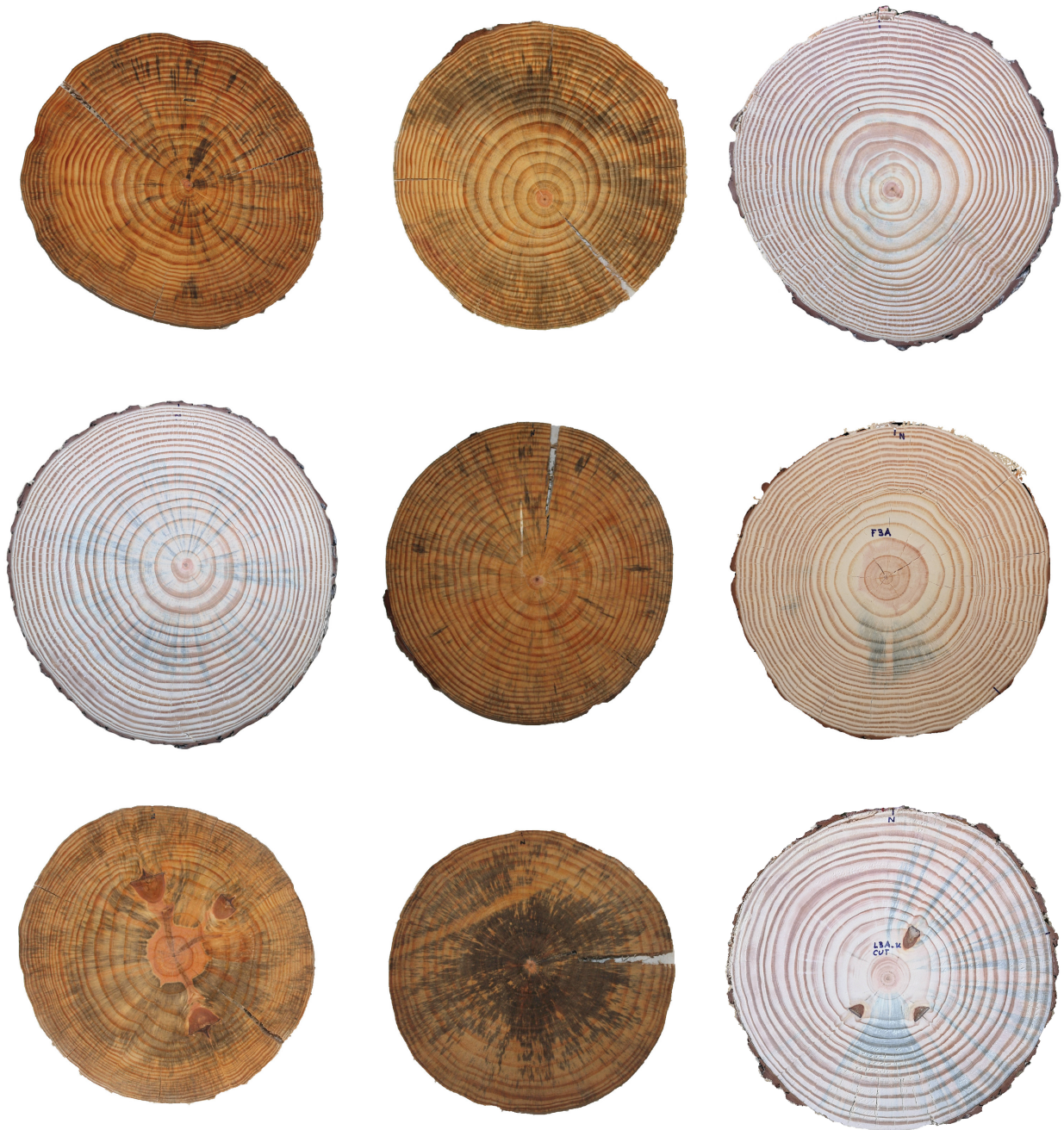


Figure 2: Some examples of images from the UruDendro dataset. Note the variability of the images and the presence of fungus (image L02b), knots (images F07b and F03c), and cracks (images F02e and L03c). The first five images are from the same tree at different heights, as the text explains in Section 6.1.

a method based on Jacobi Sets to detect the ring pattern and pith location [11]. All these methods rely on detecting the edges corresponding to the tree rings and different strategies to reconstruct the pattern. In all cases, the pith is the center of a general structure. Most of these works were tested against a few images (ranging from 7 to 20). Unfortunately, the code and used images are unavailable in these cases for testing and comparing the results with other methodologies.

Deep learning approaches have become more popular in recent years and have naturally been applied to this problem. Still, the scarcity of labeled data for a given species is a significant problem in the area, as the methods must be tailored to the particularities of each species. Gillert et al., [7] proposed a method for cross-section tree-ring detection named Iterative Next Boundary Detection Network (INBD) but applied it to high-resolution images of shrub cross-sections specially conditioned for microscopy observation. In this case, the images are not only of a particular species, but also the microscopic resolution introduces specific characteristics. Starting from the pith, the method infers the annual ring at each iteration step, detecting ring by ring from the medulla to the tree’s bark. A problem can arise if an intermediate ring is badly processed. In those cases, the error propagates and affects all the rings outward. The method was trained and tested on images obtained under the specific conditions of microscopic images of shrub species. This is the unique method for which we have access to the code, allowing us to compare it with our approach. In Section 6.5, we illustrate the results of applying their model to our datasets, training their method for our particular images.

Besides the INBD method, most deep-learning-based approaches are applied to core images. For example, recently, Polek et al.[15] applied a deep learning approach to process cores of coniferous species. Fabijańska et al. proposed both a classic image-processing approach [6] (based on the linking of image gradient peak detected pixels) and a convolutional neural network one [5] for detecting tree rings over core images. Comparing both methods, they reported a precision of 43% and a recall of 51% for the classical approach, a precision of 97%, and a recall of 96% for the deep learning one. Without the code or the data, it is impossible to verify these claims with other species or datasets (their experiments concern three ring-porous wood species).

In short, deep learning-based methods are almost all for cores, and the absence of labeled databases makes it difficult to use them on complete slices. Classical methods are generally based on edge detection and build rings out of them. Most reported methods lack the code or the data to verify their claims. Still, their analysis leads to the assumption that the presence of perturbations such as fungus, cracks, and knots strongly affects the performance because the construction of each ring depends on the previous ones. Therefore, an error in the pith or rings close to the center propagates to the rest of the structure.

3 Proposed Approach

In this section, we present the main ideas of the method for tree-ring delineation over RGB cross-section images, called CS-TRD for Cross-Section Tree-Ring Detector.

3.1 Assumptions

Our tree-ring detection algorithm is heavily based on the structural characteristics of the problem:

- The use of the whole horizontal cross-section of a tree (slice) instead of a wood dowel (or core), as most dendrochronology approaches do.
- The following properties generally define the rings on a slice:

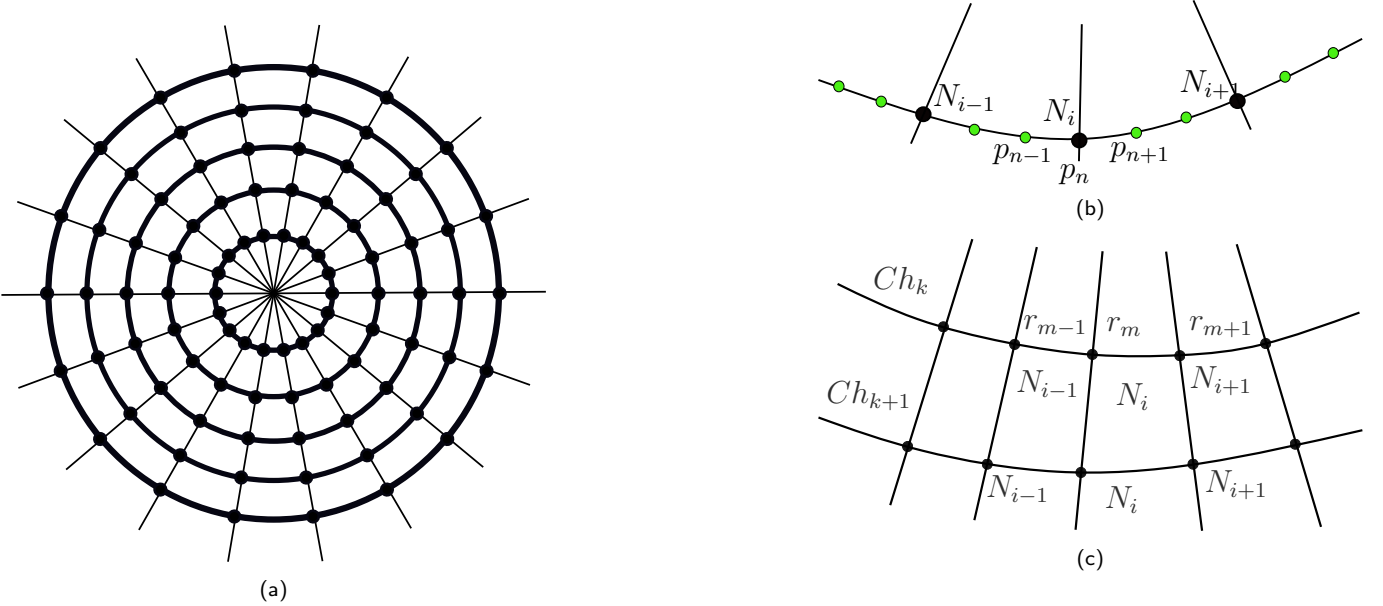


Figure 3: (a) The whole structure, called *spider web*, is formed by a *center* (which corresponds to the slice pith), N_r *rays* (in the drawing $N_r = 18$) and the *rings* (concentric curves). In the scheme, the *rings* are circles, but in practice, they can be (strongly) deformed as long as they don't intersect another *ring*. Each ray intersects a ring only once in a point called *node*. (b) A curve is a set of connected *points* (small green dots). Some of those *points* are the intersection with *rays*, named *nodes* (black dots). A chain is a set of connected *nodes*. In this case, the *node* N_i is the *point* p_n . (c) Each *Chain* Ch_k and Ch_{k+1} , intersects the *rays* r_{m-1} , r_m and r_{m+1} in *nodes* N_{i-1} , N_i and N_{i+1} .

1. The rings are roughly concentric, even if their shape is irregular. This means that two rings can't cross.
2. Several rays can be traced outwards from the slice pith. Those rays will cross each ring only once.
3. We are interested only in the rings corresponding to the latewood to earlywood transitions, namely the *annual rings*.

The principal idea of the method proposed in this work is the definition and use of a general structure formed by the rings, as explained in Section 3.2.

3.2 Definitions

To explain the approach, we need some naming definitions; see Figure 3. We call *spider web* the global structure of the tree-rings we are searching for, which is depicted in a general way in Figure 3.a. It comprises a *center*, associated with the slice's pith, which is the origin of a certain number of *rays*. The *rings* are concentric and closed curves that do not cross each other. Each *ring* is formed by a *curve* of connected points. Each *ray* crosses a *curve* only once. The *rings* can be viewed as a *curve* of points with *nodes* in the intersection with the *rays*. A *chain* is a set of connected *nodes*. As shown in Figure 3.b, a *curve* is a set of chained nodes (small green dots in the figure, noted P_i). Depending on the position of the *curve* concerning the *center*, some of those *points* are *nodes* (larger black dots in the figure, denoted N_i hereafter). The larger the number N_r of *rays*, the better the precision of the reconstruction of the *rings*. We fix $N_r = 360$. Note that this is the ideal setting. In actual images, *rings* can disappear without forming a closed curve, the *rings* can be strongly deformed, etc.

Figure 3.c illustrates the nomenclature used in this paper: *Chains* Ch_k and Ch_{k+1} , intersect the *rays* r_{m-1} , r_m and r_{m+1} in *nodes* N_{i-1} , N_i and N_{i+1} . To explain the method, we use this terminology.

Chains merge to form a *ring*. The *rays* determine a sampling of the *curves*, producing *chains*.

3.3 Approach

The method takes as input an image of the disk without background and the biological center of the disk (pith) (see Figure 4.b) and returns the annual rings (see Figure 4.i). Figure 4 illustrates the output of each stage of the method, which are fully described in Section 4.

Briefly, the method works as follows: from the center (disk pith), rays are traced (see Figure 3.a). The Canny edge detection method is then applied to the image (see Figure 4.d), and by calculating the angle between the edge normals and the rays, most of the edges that do not belong to the latewood to earlywood transitions are eliminated. At the end of this filtering stage, we obtain both noisy edges and the edges of the rings we are looking for; additionally, some edges may be missing because they were not detected (see Figure 4.e). Until now, the method is similar to the one proposed by Cerdà et al. [1]; the more challenging step is how the pixels belonging to the edges are grouped to form rings.

In the next stage, the edges obtained in the previous phase enforce the *spider web* structure, which describes the general properties of the annual rings. To achieve this, all edges are subsampled using the rays of *spider web*: for each edge, we only retain the intersections between it and the respective rays (the nodes), forming what we call chains (see Figure 4.f).

The final stage involves grouping all chains that belong to the same ring by imposing the SpiderWeb structure through a smoothness condition (see Figure 4.g, Figure 4.h and Equation (5)). The chain grouping is performed iteratively to connect chains near areas with stronger edge information. Once no more chains are connected in the current neighborhood, the method moves on to the next region with strong edge information. This iterative process, which prioritizes edge information along with the smoothness condition, is the main contribution of our method to the community. Now, we describe the method in detail.

4 Algorithm

Algorithm 1 depicts the CS-TRD method and Figure 4 illustrates its intermediate results. The input is an image of a tree slice. First, we subtract the background, applying a deep learning-based approach [16] based on a two-level nested U-structure (U^2Net).

Given the image without a background as shown in Figure 4.b, we must find the set of pixel chains representing the annual rings (dark to clear transitions). We need the center $c = (cy, cx)$ of the *spider web* (the tree’s pith) as input. This fundamental point can be manually marked or can be automatically detected [2]. Here, we consider that this point is given (in the demo, both options are available). Note that the values of parameters α , N_r , and m_c are fixed once and for all.

4.1 Preprocessing

The first step in Algorithm 1 is to preprocess the input image to increase the method’s performance. We resize the image to a fixed 1500×1500 pixels size via Lanczos interpolation, then convert it to grayscale, and a histogram equalization is applied (Figure 4.c).

4.2 Canny-Devernay edge detector

Line 2 of Algorithm 1 corresponds to the edge detection stage. We apply the sub-pixel precision Canny Devernay edge detector [3, 8]. The output of this step is a list of pixel chains corresponding

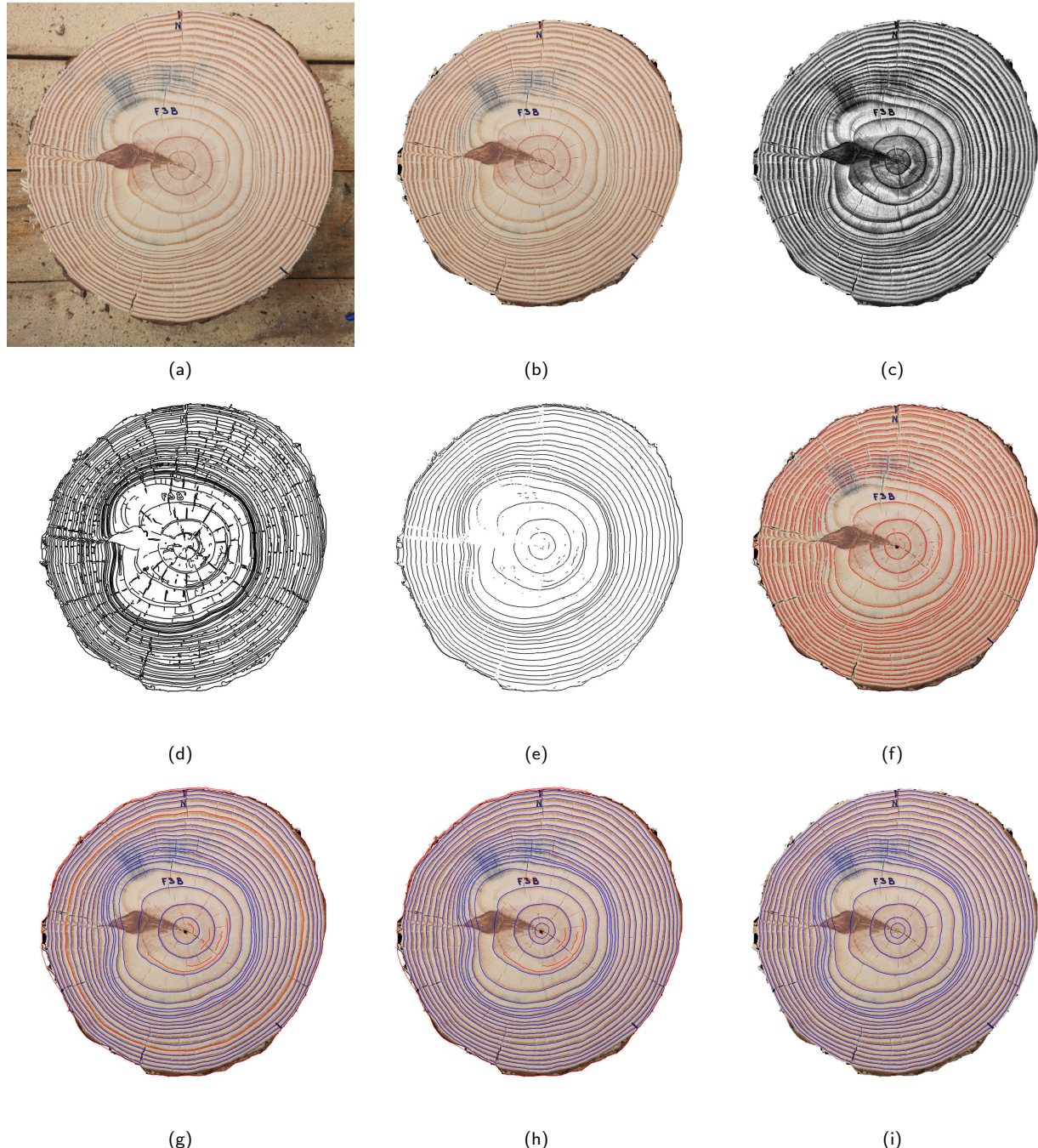


Figure 4: Principal steps of the CS-TRD algorithm: (a) Original image, (b) Background subtraction, (c) Pre-processed image (resized, equalized, grayscale conversion), (d) Canny Devernay edge detector, (e) Edges filtered by the direction of the gradient, (f) Detected chains, (g) Connected chains, (h) Post-processed chains and (i) Detected tree-rings.

Algorithm 1: Tree-ring detection algorithm

Input: Im_{in} , // segmented input image. Background pixels are set to 255 (white)
 cy, cx , // pith's coordinates, in pixels: center of the *spider web*
 σ , // Canny edge detector gaussian kernel parameter
 $height, width$, // dimensions of the image after the resize step
 α , // threshold on the collinearity of the edge filtering
 N_r , // number of rays
 m_c // minimum chain length
Output: A json object l_rings , each element is a closed *chain* representing a tree-ring.

```

1  $Im_{pre}, cy, cx \leftarrow \text{preprocessing}(Im_{in}, height, width, cy, cx)$ 
2  $m\_ch_e, G_x, G_y \leftarrow \text{canny\_deverney\_edge\_detector}(Im_{pre}, \sigma)$  // described in [8]
3  $l\_ch_f \leftarrow \text{filter\_edges}(m\_ch_e, cy, cx, G_x, G_y, \alpha, Im_{pre})$ 
4  $l\_ch_s, l\_nodes_s \leftarrow \text{sampling\_edges}(l\_ch_f, cy, cx, N_r, m_c, Im_{pre})$ 
5  $l\_ch_c, l\_nodes_c \leftarrow \text{connect\_chains}(l\_ch_s, l\_nodes_s, cy, cx)$ 
6  $l\_ch_p \leftarrow \text{postprocessing}(l\_ch_c, l\_nodes_c)$ 
7  $l\_rings \leftarrow \text{chain\_to\_labelme\_json}(l\_ch_p, height, width, cy, cx, Im_{in})$ 
8 return  $l\_rings$ 

```

to the image edges. Besides some noise-derived ones, we can group those edges into three classes:

- $Edges_T$: produced by the tree growing process. It includes the edges that form the rings. Considering a pith outward direction, they can be of two types: those produced by early wood to late wood transitions (clear to dark) and latewood to early wood transitions (dark to clear). We are interested in detecting the former ones, hereon called annual rings.
- $Edges_R$: radial edges produced by cracks, fungi, or other phenomena.
- Other edges produced by wood knots and noise.

The gradient vector is normal to the edge and encodes the local direction and sense of the transition. The Canny Devernay filter produces the G_x and G_y matrices with x and y gradient components, respectively, and m_ch_e , the matrix of edge chains, in which successive rows list the coordinates (x, y) of the chained pixels of a given edge, and the row $[-1, -1]$ signals the end of an edge chain.

The Canny Devernay edge detector has three parameters: The standard deviation of the Gaussian kernel σ , and the gradient modulus thresholds th_{low} and th_{high} , associated with the threshold with hysteresis filtering on the edge points. We only adjust the parameter σ ; the other two are fixed (see Section 6.3.1). Figure 4.d show the output of this stage. We slightly modify the Canny Devernay filter IPOL implementation [8] to get the matrices G_x and G_y as output.

4.3 Filtering the edge chains

Line 3 of Algorithm 1 corresponds to the edge filtering stage. Given the center $c = (cy, cx)$ and a point p_i over an edge *curve*, the angle $\delta(c\vec{p}_i, \vec{G}_{p_i})$ between the vector $c\vec{p}_i$ and the gradient vector \vec{G}_{p_i} at the the point p_i is given by:

$$\delta(c\vec{p}_i, \vec{G}_{p_i}) = \arccos \left(\frac{c\vec{p}_i \times \vec{G}_{p_i}}{\|c\vec{p}_i\| \|\vec{G}_{p_i}\|} \right) \quad (1)$$

We filter out all *points* p_i for which $\delta(c\vec{p}_i, \vec{G}_{p_i}) \geq \alpha$. We fix $\alpha = 30$ degrees.

Two edge groups are filtered out: early wood transitions of the *Edges_T* set gradients, which point inward, and *Edges_R* set gradients, roughly normal to the *rays*. The algorithm produces the list l_ch_f , including mainly the ring's edges and a disk border chain in the last position. Figure 4.e show the output of this stage.

4.4 Sampling edges

Line 4 of Algorithm 1, is the edge sampling stage which produces the *nodes* depicted in Figure 3.b. We sample each *curve* of the l_ch_f list using the number of rays N_r . The algorithm has two parameters: N_r (360 by default) and m_c , the minimum number of nodes in a *chain*. Every *chain* has two endpoints, so we fix $m_c = 2$. The algorithm produces two lists: l_ch_s (of **Chain** objects) and l_nodes_s (of **Nodes** objects), which includes the nodes of all chains. These lists include two artificial *chains*, one of type *center* with N_r nodes with the exact pith coordinates but different angular orientations, and one corresponding to the border. The inclusion of these artificial chains is beneficial for the connecting chain stage. The attribute *type* of the object **Chain** identifies if it is an artificial or a standard chain.

Figure 4.f shows this stage output. Standard chains are in red, and center and border chains are in black. Due to the sampling, there are fewer chains than edges. Figure 4.e has more (noisy) curves around the pith than Figure 4.f. Some small curves whose sampled length is shorter than m_c are discarded. In that sense, this parameter filters out "short" chains.

Every chain has two endpoint nodes, A and B. Endpoint A is always the furthest node clockwise, while endpoint B is the most distant node counterclockwise. We use the concepts of *outward* and *inward* (concerning a given endpoint) in the chain attributes. Given the corresponding *ray* of a *chain* endpoint, we find the first *chain* that intersects it going from the chain to the center along the *ray* (named *inward*) and the first *chain* that intersects that *ray* moving away from the center (named *outward*), as shown in Figure 5. Chains are superposed over the gray-level image. The ray at endpoint A is blue, and the nodes are red and lie at the intersection between the rays and the edges. Orange and yellow chains are the *visible* ones for the black chain at endpoint A (outward and inward, respectively).

We use three metric distances between chains. Given $EndPoint_j$ for the current chain Ch_j , and $EndPoint_k$ for chain Ch_k , distances are defined as:

- **Euclidean** defined as

$$d_e = \sqrt{(x_j - x_k)^2 + (y_j - y_k)^2} \quad (2)$$

Where (x_j, y_j) and (x_k, y_k) are the cartesian coordinates of $EndPoint_j$ and $EndPoint_k$.

- **Radial Difference** defined as

$$d_{rd} = \|r_j - r_k\| \quad (3)$$

r_j is the Euclidean distance between $EndPoint_j$ and the pith center, and r_k is the Euclidean distance between $EndPoint_k$ and the pith center.

- **Angular** Given the endpoints ray support angle, θ_j and θ_k , this distance is defined as

$$d_a = (\theta_j - \theta_k + 360) \bmod 360 \quad (4)$$

Where θ_j and θ_k are the ray's direction supporting $EndPoint_j$ and $EndPoint_k$ (both in degrees), respectively, *mod* refers to the module operation.

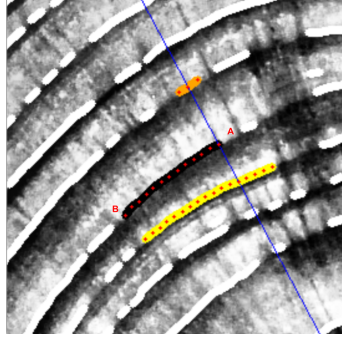


Figure 5: A given chain (in black) with two endpoints A and B. Its nodes (in red) appear at the intersection between the Canny Devernay curve and the rays. The ray at endpoint A is in blue. Other chains detected by Canny Devernay are in white. Endpoint A's inward and outward chains are in yellow and orange, respectively.

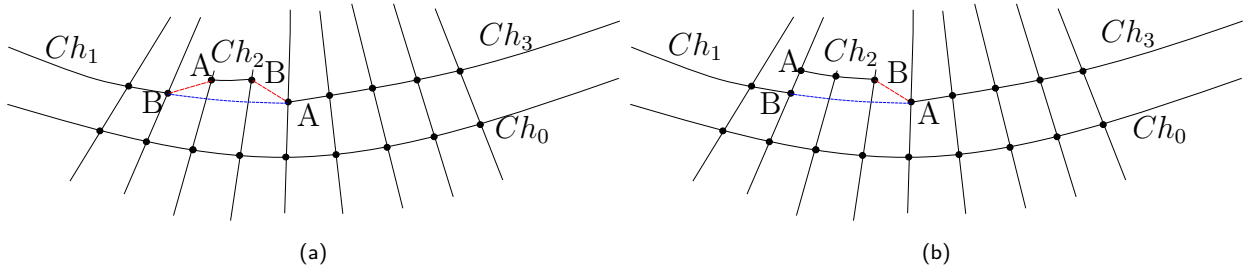


Figure 6: An illustration of the *connectivity* issue. (a) The question is if endpoint A of Ch_3 must be connected to endpoint B of Ch_2 (red dashed line) or to endpoint B of Ch_1 (blue dashed line). In figure (b), the same question can be posed for the connection between endpoint B of Ch_1 and endpoint A of Ch_2 . This connection is forbidden because Ch_1 and Ch_2 intersect (the endpoints are on the same ray). Note that we represent the connections by line segments for clarity, but these are curves in the image space, as we interpolate between *chain* endpoints in polar geometry.

4.5 Connect chains

We must now group these chains to form the rings (Line 5 of Algorithm 1). As this section is one of the main parts of the algorithm, we will divide it into two subsections: one that explains the general idea of chain connection and another that details the algorithms themselves.

4.5.1 General Logic of Chain Connection

The input of the algorithm is a set of chains. Some of these chains are spurious, produced by noise, small cracks, knots, etc., but most are part of the desired rings, as seen in Figure 4.f.

In general, several chains form a ring. To connect them, we must decide if the endpoints of two given chains can be connected, as illustrated by Figure 6.a. We use a support chain (Ch_0 in the figure) to determine if those chains must be connected.

To group chains that belong to the same ring, we proceed as follows:

1. We order all the chains by length and begin by processing the longest, which we call *Chain support*, Ch_i . Once we finish merging all the possible *candidate chains* related to that one (the set $candidate_{Ch_i}$), we do the same with the next longest *chain*, and so on. The reason for processing the longest chains first is that longer chains contain more edge information and more information about the tree ring structure, giving more robust results. Longer chains are more likely to be an edge belonging to an annual tree ring. Since consecutive rings have similar shapes, this iteration method propagates the shape of the longer chains.
2. We find the chains that are visible from the *Chain support* inwards (i.e., in the direction from

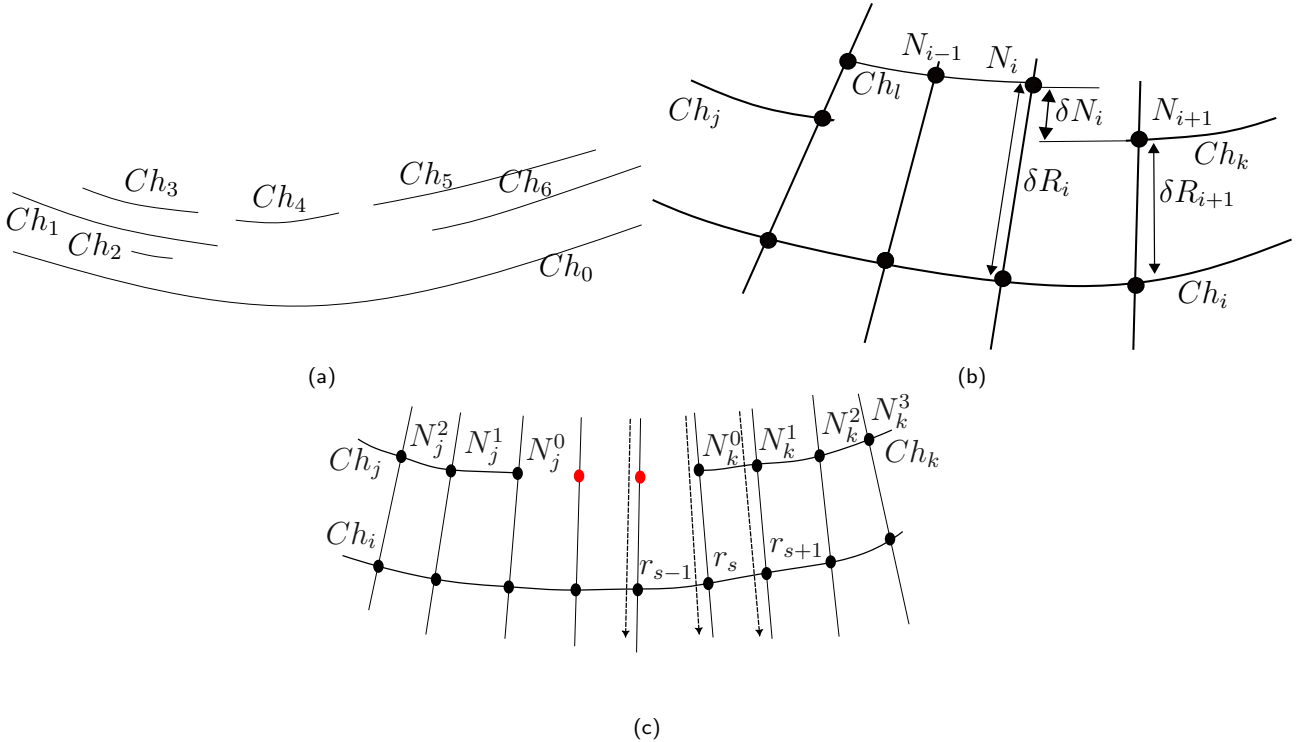


Figure 7: Connectivity nomenclature. (a) For the *chain support* Ch_0 , the set of *chain candidates* is formed by Ch_1 , Ch_2 , Ch_4 , Ch_5 and Ch_6 . *Chain* Ch_3 is shadowed by Ch_1 but Ch_5 is not shadowed by Ch_6 because at least one endpoint of Ch_5 is visible from Ch_0 . Note that a *chain* becomes part of the *candidate chains* set if at least one of its endpoints is visible from the *chain support*. (b) Quantities used to measure the connectivity between *chains*. δR_i is the radial difference between two successive *chains* along a *ray* R_i and δN_i is the radial difference between two successive *nodes* N_i and N_{i+1} . Note that these nodes can be part of the same *chain* or be part of two different *chains* that may be merged. Ch_i is the *support chain*. Ch_i visible chains are Ch_j , Ch_l and Ch_k . Chains Ch_j and Ch_k satisfy similarity conditions. (c) Chains Ch_j and Ch_k are candidates to be connected, and Ch_i is the *support chain*. N_j^n (N_k^n) are the nodes of Ch_j (Ch_k), with $n = 0$ for the endpoint to be connected, and r_s represents the radial distance to the center of $Node^s$. In red are the nodes created by an interpolation process between both endpoints.

Chain support to the center). Here, *visible* means that a *ray* that goes through one *candidate chain* endpoint crosses the *chain support* without crossing any other *chains* in between. The set of *candidate chains* of the *Chain support* Ch_i is named $candidates_{Ch_i}$. In Figure 7.a this set is $candidates_{Ch_0} = \{Ch_1, Ch_2, Ch_4, Ch_5, Ch_6\}$. *Chain* Ch_3 is shadowed by Ch_1 and Ch_5 is not shadowed by Ch_6 because at least one of its endpoints are visible from Ch_0 . The same process is made for the chains visible from the *Chain support* outwards.

3. We explore the set $candidates_{Ch_i}$ searching for connections between them. By construction, the *chain support* is not a candidate to be merged in this step. From the endpoint of a chain, we move forward angularly. The next endpoint of a nonintersecting *chain* in $candidates_{Ch_i}$ is a candidate to be connected to the first one. We say that two *chains* intersect if there exists at least one *ray* that crosses both *chains*. For example, in Figure 7.a, Ch_6 intersects with Ch_5 but not with Ch_4 .
4. To decide if both chains must be connected, we must measure the *connectivity goodness* between them, combining four criteria:
 - (a) *Radial tolerance for connecting chains*. The radial difference between the distance from each chain to be merged (measured at the endpoint to be connected) and the support chain must be small. For example, in Figure 7.b, if we want to connect node N_i of Ch_l

and node N_{i+1} of Ch_k , we must verify that

$$\delta R_i * (1 - Th_{Radial_tolerance}) \leq \delta R_{i+1} \leq \delta R_i * (1 + Th_{Radial_tolerance})$$

Where $Th_{Radial_tolerance}$ is a parameter of the algorithm. We call this condition *RadialTol*.

- (b) *Similar radial distances of nodes in both chains.* For each chain, we define a set of nodes. For the chain Ch_j , this set is $N_j = \{N_j^0, N_j^1, \dots, N_j^{n_{nodes}}\}$ where n_{nodes} is the number of nodes to be considered, fixed to $n_{nodes} = 20$. See Figure 7.c. We use the whole chain if it is shorter than n_{nodes} . We measure δR_i , the radial distance between each node in the given chain and the corresponding node (same ray) in the support chain, as illustrated in Figure 7.b. This defines a set for each considered chain j and k : $Set_j = \{\delta R_j^0, \dots, \delta R_j^{n_{nodes}}\}$ and $Set_k = \{\delta R_k^0, \dots, \delta R_k^{n_{nodes}}\}$. We calculate its mean and standard deviation $Set_j(\mu_j, \sigma_j)$ and $Set_k(\mu_k, \sigma_k)$. This defines a range of radial distances associated with each chain: $Range_j = (\mu_j - Th_{Distribution_size} * \sigma_j, \mu_j + Th_{Distribution_size} * \sigma_j)$ and $Range_k = (\mu_k - Th_{Distribution_size} * \sigma_k, \mu_k + Th_{Distribution_size} * \sigma_k)$, where $Th_{Distribution_size}$ is a parameter. There must be a non-null intersection between both distributions to connect both chains: $Range_j \cap Range_k \neq \emptyset$. We call this condition *SimilarRadialDist*.
- (c) *Regularity of the derivative.* Given two chains Ch_j and Ch_k which can be connected, let's call Ch_{jk} the set of interpolated nodes between them (Figure 7.c). The new virtual chain created by the connection between Ch_j and Ch_k will encompass the nodes of those two chains and Ch_{jk} . The parameter *derivFromCenter* controls how are estimated the interpolated nodes between two chains, as the ones in red in Figure 7.c. If *derivFromCenter* = 1, ray angle and radial distance from the center are used to estimate the position of the interpolated nodes. If its value is 0, the estimation is made by measuring the radial distance to the support chain. To test the regularity of the derivative, we define a set of nodes for each concerned chain. For the chain Ch_j , this set is $\{N_j^0, N_j^1, \dots, N_j^{n_{nodes}}\}$ where $n_{nodes} = 20$ is the number of nodes to be considered. If the chain is shorter, we use all nodes. We compute the centered derivative in each node for all chains, $\delta N^s = \frac{\|r_{s+1} - r_{s-1}\|}{2}$, where r_s is the radial distance of the node N^s to the center (i.e., the Euclidean distance between the node and the center). The set of the existing chains nodes is $Der(Ch_j, Ch_k) = \{\delta N_j^0, \dots, \delta N_j^{n_{nodes}}, \delta N_k^0, \dots, \delta N_k^{n_{nodes}}\}$. The condition *RegularDeriv* is asserted if the greatest derivative in the interpolated chain is less or equal to the greater derivative in the neighboring chains, with tolerance $Th_{Regular_derivative}$:

$$\max(Der(Ch_{jk})) \leq \max(Der(Ch_j, Ch_k)) \times Th_{Regular_derivative}$$

- (d) *Non-Overlapping Chain.* Finally, no other chain must exist between the chains to be connected. If another chain exists in between, it must be connected to the closer one. For example, in Figure 7.a, it is impossible to connect chains Ch_3 and Ch_5 because between them appear Ch_4 . We call this condition *ExistChainOverlapping*.

Summarizing, in order to connect chains Ch_j and Ch_k , the following condition must be met:

$$\mathbf{not} ExistChainOverlapping \wedge RegularDeriv \wedge (SimilarRadialDist \vee RadialTol) \quad (5)$$

where \vee and \wedge stands for the logical *or* and *and* symbols, respectively, and the symbol **not** stands for the *not* operator.

The method iterates, searching for connectivity between chains over different neighborhood sizes. The parameter *NeighbourhoodSize* defines the maximum allowed distance, measured in degrees, for connecting two chains.

We iterate this process for the whole image nine times. In the first iteration, there are a lot of small chains, but in the second and third iterations, the concerned chains are already more extended and less noisy. As the merging process advances, we can relax the parameters to connect more robust chains. Table 1 summarizes the parameters used in each iteration.

| | 1 | 2 | 3 | 4 | 5 | 6 | 7 | 8 | 9 |
|----------------------------|-----|-----|-----|-----|-----|-----|-----|-----|-----|
| $Th_{Radial_tolerance}$ | 0.1 | 0.2 | 0.1 | 0.2 | 0.1 | 0.2 | 0.1 | 0.2 | 0.2 |
| $Th_{Distribution_size}$ | 2 | 2 | 3 | 3 | 3 | 3 | 2 | 3 | 3 |
| $Th_{Regular_derivative}$ | 1.5 | 1.5 | 1.5 | 1.5 | 1.5 | 1.5 | 2 | 2 | 2 |
| $NeighbourhoodSize$ | 10 | 10 | 22 | 22 | 45 | 45 | 22 | 45 | 45 |
| $derivFromCenter$ | 0 | 0 | 0 | 0 | 0 | 0 | 1 | 1 | 1 |

Table 1: Connectivity Parameters. Each column is the parameter set used on that iteration.

5. We proceed in the same manner in the outward direction.

4.5.2 Detailed Description of the Algorithms

Algorithm 2 depicts the chain connection step’s logic, described in the former section. It is iteratively called from an external function (Line 5 of Algorithm 1) with the parameter values defined in Table 1 columns. Chains produced at one iteration become the input chains for the next one.

As was mentioned, the logic for connecting chains is based on iterating over the *support chain*. For each one, the set of visible chains is selected. The logic for selecting the support chain in each iteration (line 1 Algorithm 2) is encapsulated in the **SystemStatus** object, which is the hub of our *system*, containing all the necessary information to operate. The *system* comprises all the chains and nodes and the intersection matrix M . This binary square matrix stores the intersection information of chains at each iteration. Rows and columns of M span the chain list. Chain Ch_j intersect chain Ch_k if $M[j, k] = 1$. We say that two chains intersect if at least one ray crosses both chains. The intersection matrix, M , is an input argument for Algorithm 2. The **SystemStatus** object updates the chains and nodes lists and the matrix M whenever two chains are connected. This update is critical for our operation and signifies that the *system* has been modified.

Algorithm 2 has a main loop from lines 2 to 19. Each iteration, the **SystemStatus** object produces the support chain (Ch_i). Support chains are iterated by following a neighborhood logic instead of sequentially going over the list to speed up the process. Given a support chain, a secondary loop (lines 5 to 18) iterates over the inward (or outward) visible chains, as described in Figure 7.a. In a third inner loop (lines 11 to 18), each candidate chain (Ch_j) is examined to find the closest chain (Ch_k) that meets the similarity goodness criteria (Equation (5)). In summary, we search for the nearest chains to endpoints Ch_k^a and Ch_k^b . Between these candidate chains, we select the closest one (Ch_k) that does not intersect with the original chain Ch_j . Then, in line 17, chains Ch_j and Ch_k are connected. Connecting two chains implies generating new nodes between them (the new chain cannot have “holes”). Once no more chains can be connected, the main loop (lines 2 to 19) exits. In line 20, we iterate over all the chains in l_ch_s , and if one has enough nodes, we complete it. The output is the lists of chains (l_ch_c), nodes (l_nodes_c), and the intersection matrix, M .

Once we have a support chain (Ch_i), we iterate over the visible chains to connect them if they meet the similarity criteria as briefly shown in Algorithm 2.

Algorithm 2: Connect Chains Main Logic

Input: l_ch_s , // chains list
 l_nodes_s , // nodes list
 M , //Binary Matrix with intersection chains info
 cy, cx , // pith's coordinates, in pixels: center of the *spider web*
 N_r , // total number of rays
Parameters:
 $th_radial_tolerance$, // Radial tolerance for connecting chains
 $th_distribution_size$, // Chains Radial Difference Standard deviations for connecting chains
 $th_regular_derivative$, // Chains Radial Derivative threshold for connecting chains
 $neighbourhood_size$, //Maximum angular distance allowed for connecting chains
 $derivative_from_center$ // Define how nodes are interpolated

Output: A list l_ch_c , where each element is a *chain*,
 l_nodes_c , where each element is a *Node*,
 M , intersection matrix updated

```

1 state ← SystemStatus( $l\_ch_s, l\_nodes_s, M, cy, cx, N_r, th\_radial\_tolerance, th\_distribution\_size,$ 
 $th\_regular\_derivative, neighbourhood\_size, derivative\_from\_center$ )
2 while state.continue_in_loop() do
3    $Ch_i \leftarrow state.get\_next\_chain()$ 
4    $l\_s\_outward, l\_s\_inward \leftarrow get\_chains\_in\_and\_out\_wards(l\_ch_s, Ch_i)$ 
5   for  $l\_candidates\_Ch_i$  in ( $l\_s\_outward, l\_s\_inward$ ) do
6      $j\_pointer \leftarrow 0$ 
7     if  $l\_candidates\_Ch_i = l\_s\_inward$  then
8       location ← "inward"
9     else
10      location ← "outward"
11     while  $length(l\_candidates\_Ch_i) > j\_pointer$  do
12        $Ch_j \leftarrow l\_candidates\_Ch_i[j\_pointer]$ 
13        $l\_no\_intersection\_j \leftarrow get\_non\_intersection\_chains(M, l\_candidates\_Ch_i, Ch_j)$ 
14        $Ch_k^b \leftarrow get\_closest\_chain\_logic(state, l\_candidates\_Ch_i,$ 
 $Ch_j, l\_no\_intersection\_j, Ch_i, location, B)$ 
15        $Ch_k^a \leftarrow get\_closest\_chain\_logic(state, l\_candidates\_Ch_i,$ 
 $Ch_j, l\_no\_intersection\_j, Ch_i, location, A)$ 
16        $Ch_k, endpoint \leftarrow select\_closest\_one(Ch_j, Ch_k^a, Ch_k^b)$ 
17       connect_two_chains(state,  $Ch_j, Ch_k, l\_candidates\_Ch_i, endpoint, Ch_i$ )
18        $j\_pointer \leftarrow update\_pointer(Ch_j, Ch_k, l\_candidates\_Ch_i)$ 
19     state.update_system_status( $Ch_i, l\_s\_outward, l\_s\_inward$ )
20    $l\_ch_c, l\_nodes_c, M \leftarrow iterate\_over\_chains\_list\_and\_complete\_them\_if\_met\_conditions(state)$ 
21 return  $l\_ch_c, l\_nodes_c, M$ 

```

The method *get_closest_chain_logic* (lines 14 and 15 of Algorithm 2) provides the closest chain, performing a dual symmetry check: if chain Ch_k is the closest to Ch_j , then the closest one to Ch_k should also be Ch_j . Algorithm 3 (function *get_closest_chain*), invoked within *get_closest_chain_logic*, search for the closest candidate chain (described in Section 4.5.1 item 3) that meet conditions described in Section 4.5.1 item 4. In line 2, all chains in the neighborhood (defined by the Ch_j endpoint and the *neighbourhood_size state* attribute) are selected. For example, given the endpoint A with an angle of 0 degrees and *neighbourhood_size* = 20, all the chains included in *l_candidates_Ch_i* with endpoint B angle in $[0 - 20, 0] = [340, 360]$ are selected and returned in ascending angular order concerning the endpoint of Ch_j . Lines 5 to 13 define the main loop. Two conditions determine an exit from the loop: either it exists a chain that satisfies conditions from Equation (5) or no chains in the set *l_sorted_chains_in_neighbourhood* satisfy the conditions. Line 7 of function *connectivity_goodness_condition* implements Equation (5).

Algorithm 3: Get closest chain

Input: *state*,
 Ch_j , // current chain
 $l_no_intersection_j$, // chains that no intersect with Ch_j , set of candidates to connect with Ch_j
 Ch_i , // support chain
location, // inward o outward position of Ch_j regarding to the support chain
endpoint, // Ch_j endpoint
 M , // intersection matrix
Output: closest chain to Ch_j that satisfies the connectivity goodness conditions.

```

1 neighbourhood_size  $\leftarrow$  state.neighbourhood_size
2 l_sorted_chains_in_neighbourhood  $\leftarrow$  get_chains_in_neighbourhood(neighbourhood_size,
   l_no_intersection_j, Ch_j, Ch_i, endpoint, location)
3 next_id  $\leftarrow$  0
4  $Ch_k \leftarrow$  None
5 while len(l_sorted_chains_in_neighbourhood)  $>$  next_id do
6   candidate_chain  $\leftarrow$  l_sorted_chains_in_neighbourhood[next_id]
7   pass_control, radial_distance  $\leftarrow$  connectivity_goodness_condition(state, Ch_j,
      candidate_chain, Ch_i, endpoint) // See Algorithm 4
8   if pass_control then
9      $Ch_k \leftarrow$  get_the_closest_chain_by_radial_distance_that_does_not_intersect(Ch_j, endpoint,
       location, radial_distance, candidate_chain, M, l_sorted_chains_neighbourhood) // See
       Figure 6.a
10    break
11  end
12  next_id  $\leftarrow$  next_id + 1
13 end
14 return  $Ch_k$ 

```

If *candidate_chain* satisfies the conditions, a chain in the subset *l_no_intersection_j* could be closer to Ch_j in terms of the connectivity goodness conditions but at a greater angular distance. This is tested in line 9 (shown in Figure 8.a). In angular terms, the closest chain to Ch_j satisfying Equation (5) is Ch_l . However, Ch_k exists, which is more similar but not the closest one in terms of angular distance (Equation (4)). To fix this, we get all the chains that intersect Ch_l and satisfy Equation (5) with Ch_j . We sort them by radial proximity to Ch_j , Equation (3), and return the best candidate chain as the closer one regarding the radial distance.

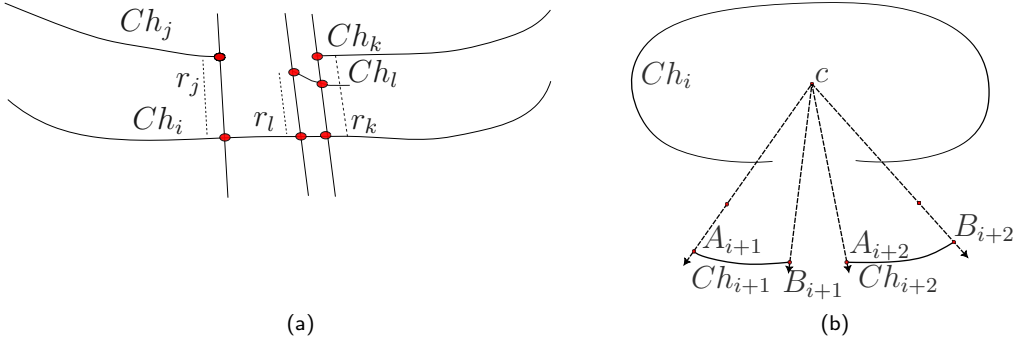


Figure 8: Chains connection. (a) Ch_i is the support chain. The candidates chains for connection with Ch_j , are Ch_k and Ch_l . The angular closest chain to Ch_j is the noisy Ch_l . Ch_k is the radially closest chain to Ch_j , these means that $\|r_j - r_k\| < \|r_j - r_l\|$. Where r_i is the chain's endpoint distance to the support chain. (b) Endpoint condition check. See the text for an explanation.

The **connectivity_goodness_condition** function is described in Algorithm 4. From lines 1 to 4, the parameters (Table 1) are extracted from the *state* object (an instance from **SystemStatus** object). In line 6, the chain size condition is verified and saved in *size_condition*. In line 7, the endpoint condition is verified. Figure 8.b shows an example of this check where Ch_i is the support chain for Ch_{i+1} and Ch_{i+2} . Endpoints A_{i+1} and B_{i+2} from chains Ch_{i+1} and Ch_{i+2} are visible. Connecting endpoints B_{i+1} and A_{i+2} is impossible because they do not belong to the chain support Ch_i angular domain. The Equation (5) condition is verified in line 8. A boolean result about the similarity condition and the absolute difference between the mean of the radial distance of the nodes associated with Ch_j and *candidate_chain* are returned. The later is defined as $distribution_distance = \|mean(radials_{Ch_j}) - mean(radials_{candidate_chain})\|$. Finally, in line 9, all conditions are verified. The function returns a boolean value for the conditions (the variable *check*) and the value of *distribution_distance*.

4.5.3 Postprocessing

This last stage aims to complete the remaining chains, relaxing the conditions even more. Many chains are closed (i.e., $size = Nr$), which we call *rings*. There are some non-closed chains (noisy or part of a ring) that, for some reason, are still incomplete. We use the information on the neighborhood chains to close or discard these remaining chains. The ideas on connecting chains are the same as those presented in the previous section.

It can remain some chains belonging to the same ring but not forming a closed chain. Often, this is due to a minor overlapping between chains (see Figure 9). To solve this problem, we cut the overlapping chains in such a way as to avoid intersections between them and then try to reconnect the resulting chains that respect the connectivity goodness conditions.

Given two closed chains containing a set of chains between them, suppose the added angular length of the non-overlapping chains between the rings is greater than 180 degrees. In that case, we consider that those chains have enough information about the ring, so we complete it by interpolating between rings and using the location of the existing chains. The chains that become part of the closed chain are the ones that meet the connectivity goodness conditions using the last column of Table 1.

4.6 Pith detection

The pith position is an input for the method. Users can set it manually or using the method proposed by Decelle et al., [2], which is at the IPOL site.

Algorithm 4: Connectivity goodness condition**Input:** *state*,*Ch_j*, // current chain*candidate_chain*, // chain closer to *Ch_j**Ch_i*, // support chain of *Ch_j* and *candidate_chain**endpoint*, // *Ch_j* endpoint**Output:** a boolean indicating if conditions are met, *distribution_distance*

```

/* Parameter extraction, from Table 1                                */
1 th_radial_tolerance ← state.th_radial_tolerance
2 th_distribution_size ← state.th_distribution_size
3 th_regular_derivative ← state.th_regular_derivative
4 derivative_from_center ← state.derivative_from_center
/* Condition checks                                              */
5 distribution_distance ← None
6 size_condition ← Chj.size + candidate_chain.size ≤ Nr
7 endpoint_conditions ← check_endpoints(Chi, Chj, candidate_chain, endpoint) // see Figure 8.b
8 similarity_condition, distribution_distance ← similarity_conditions(state,
th_radial_tolerance, th_distribution_size, th_regular_derivative, derivative_from_center, Chi,
Chj, candidate_chain, endpoint) // Equation (5)
9 check ← size_condition and endpoint_condition and similarity_condition
10 return check, distribution_distance

```

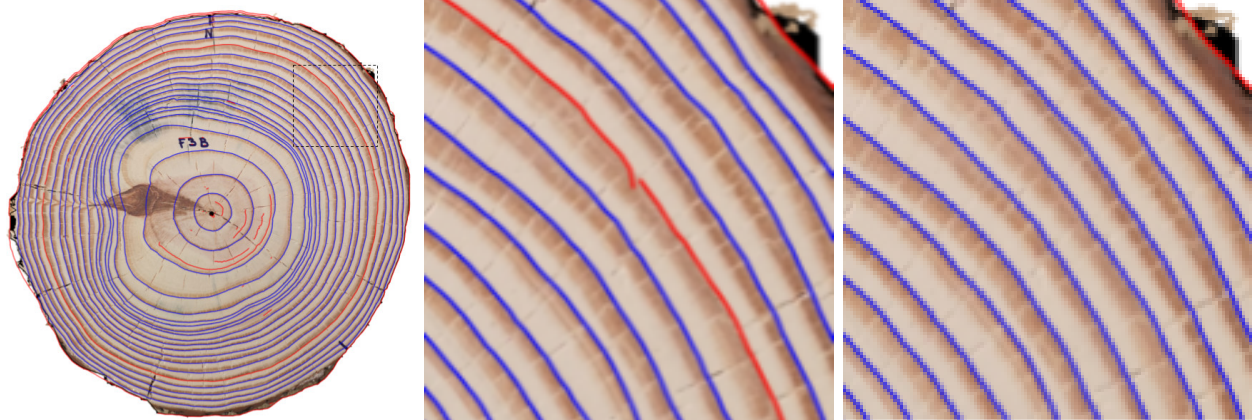


Figure 9: a) F03d disk after the connecting stage. b) There is a ring that cannot be closed because of chain intersection issues. c) The ring is closed after the postprocessing stage.

| | stage | Parameter | Description | Default |
|----------|------------------------------|--------------------------------|-------------------------------------|------------|
| Basic | Edges detector | <code>-sigma</code> | Gaussian filtering σ | 3 |
| | Preprocessing | <code>-height</code> | Rezised image height | None |
| | | <code>-width</code> | Rezised image width | None |
| | Filtering, sampling, connect | | Pith Position | Required |
| Advanced | Edges detector | <code>-th_low</code> | Gradient threshold low | 5 |
| | | <code>-th_high</code> | Gradient threshold high | 15 |
| | Edges filtering | <code>-alpha</code> | Collinearity threshold (α) | 30° |
| | Sampling | <code>-nr</code> | Number of rays (N_r) | 360 |
| | | <code>-min_chain_lenght</code> | Minimum chain length | 2 |

Table 2: Method parameters. The user can modify basic parameters in the demo.

5 Implementation details.

The implementation was made in Python 3.11. The *readme.md* file on the code repository contains all the information needed to run the code.

The demo requires, as input, an image of a tree slice and the pith position.

Table 2 summarizes the method parameters, which the user can modify if needed. As output, the method returns a JSON file with the tree-rings position in Labelme format [17].

6 Experiments and Results

6.1 Datasets

We use two datasets to evaluate the CS-TRD method.

The first one (**UruDendro**) is an online database [12] with images of cross-sections of fourteen commercially grown *Pinus taeda* trees from northern Uruguay. These trees are 13 to 24 years old and were collected in February 2020. The cross-sections are between 5 and 20 cm thick and were dried at room temperature without further preparation, which resulted in the development of radial cracks and blue fungus stains. Surfaces were smoothed with a handheld planer and a rotary sander. The dataset consists of 64 images of different resolutions, ranging between 1000 and 3000 pixels in width. It contains challenging features for automatic ring detection, including varying illumination and surface preparation, fungal infection (blue stains), knots, missing bark and interruptions in outer rings, and radial cracking. At least two experts annotate the images using the Labelme tool [17]. Figure 2 shows some images from the dataset.

The second dataset (**Kennel**) is proposed in [10], which made available a public set of 7 (1280x1280 pixels) images of *Abies alba* along with a method for detecting tree rings (the code is not available). We labeled the dataset with the same procedure as the **UruDendro** dataset as we could not process the annotations given by the authors.

6.2 Metrics

To assess the method, we developed a metric based on the one proposed by Kennel et al. [10]. To determine if a ring is detected, we define a ring influence area as the set of pixels closer to that ring. For each ray, the frontier is the midpoint between the nodes of consecutive ground truth (GT) rings.

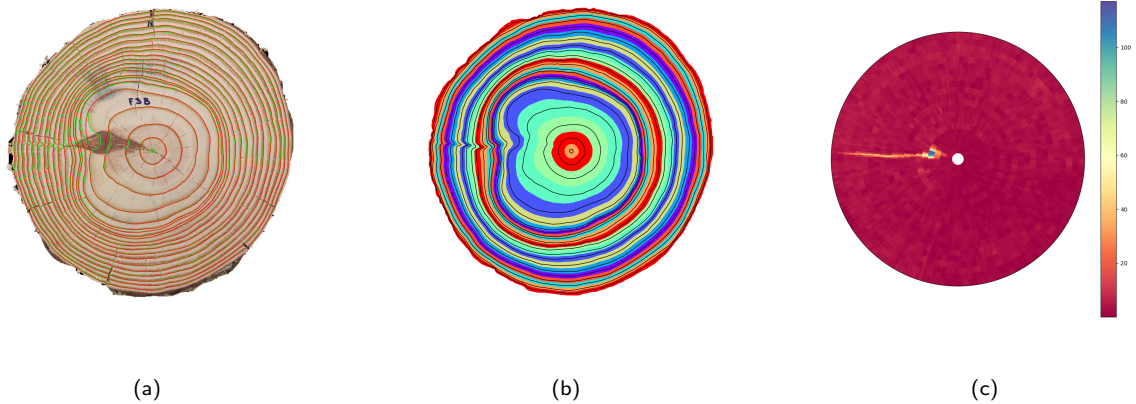


Figure 10: Measuring the error of automatic detections for image F03d: (a) In green, the GT; in red, the detections produced by the method. (b) Areas of influence of the GT rings. (c) Absolute error, in pixels, between the detections and the GT.

Figure 10.b show the influence area for rings in disk F03d. Figure 10.a shows the detections (in red) and GT marks (in green) for the same image.

The influence region associates a detected curve with a GT ring. In both cases, nodes are associated with the N_r rays. Given a GT ring, we assign it to the nearest detection using:

$$Dist = \sqrt{\frac{1}{N_r} \sum_{i=0}^{N_r-1} (dt_i - gt_i)^2} \quad (6)$$

Where i represents the ray direction, dt_i is the radial distance (Equation (3)) of detected node i , and gt_i is the radial distance (Equation (3)) of the corresponding GT node i .

The closest detection may be far from the corresponding GT ring. To match a detected curve with a GT ring, it is essential to ensure that the identified chain is the closest one to the ring and that it is sufficiently close. We utilize the influence area of each GT ring (Figure 10.b). Upon detecting a curve, if the proportion of nodes within that chain that falls within the influence area of the nearest ring exceeds a specified threshold parameter ($th_pre = 60\%$, see Section 6.3.3), we assign the detected curve to the corresponding GT ring. If it falls below the threshold, the detection is not associated with any GT ring. In other words, for a detected curve to be assigned to a GT ring and considered a true positive, at least 60% of its nodes must be within the influence area of that GT ring.

We define the absolute error $A\epsilon_i$ (in pixels) for the *node* i as the absolute difference in pixels between the GT ring and the detected ring associated with it:

$$A\epsilon_i = |r_i^d - r_i^{GT}|$$

Where r_i^d is the radial distance from the center to node i of the detected ring, and r_i^{GT} is the same for the GT ring. Figure 10.c shows the absolute error between the GT and the detected rings assigned to them. Red represents a low error, while yellow, green, and blue represent a higher error. As can be seen, the error is concentrated around the knot, affecting the precise detection of some rings.

Once all the detected chains are matched with the GT rings, we calculate the following values:

1. True Positive (TP): when the identified closed chain and the GT ring match.

2. False Positive (FP): when the identified closed chain doesn't match any GT ring.
3. False Negative (FN): when a GT ring doesn't match any detected closed chain.

Precision is given by $P = \frac{TP}{TP+FP}$, Recall by $R = \frac{TP}{TP+FN}$ and the F-Score by $F = \frac{2PR}{P+R}$.

6.3 Experiments

This section presents some experiments to help us better understand the method and its limitations.

Table 3 presents the metric results for the optimal values of σ and image resolution on both datasets. For example, CS-TRD fails to detect one ring in the image *F03d* ($FN = 1$), and the other rings are correctly detected, leading to the displayed values of P , R , and F . The table also compares the mean execution time by image and the RMSE error in pixels (Equation (6)) between the detected and GT rings. All experiments used an Intel Core i5 10300H workstation with 16GB of RAM. These are very good results, considering the data diversity and the presence of perturbations.

| Dataset | Image Size (pixels) | σ | P | R | F | RMSE | Execution Time (sec.) |
|-----------|---------------------|----------|------|------|------|------|-----------------------|
| UruDendro | 1500x1500 | 3.0 | 0,95 | 0,86 | 0,89 | 5.27 | 17.3 |
| Kennel | 1500x1500 | 2.5 | 0,97 | 0,97 | 0,97 | 2.4 | 11.1 |

Table 3: Mean performance and execution time for both datasets' at the optimal σ and image resolution.

6.3.1 Edge detector optimization stage

The algorithm heavily relies on the edge detector stage. In the first experiment, we test different σ values for the Canny Devernay edge detector to get the one that maximizes the F-Score for the UruDendro dataset. This dataset shows significant variations in image resolution, allowing us to study the overall performance with different input image dimensions. The results are presented in Figures 11.a and 11.b. We compute the average F-Score for the original image sizes and then scale all images in the dataset to 640×640 , 1000×1000 , and 1500×1500 pixels. The best result was achieved for the size 1500×1500 with $\sigma = 3.0$. The execution time varies with the image size. The average execution time for the 1500×1500 size is 17 seconds. The execution time decreased as σ increased because fewer edge chains were detected. Results for the same experiment on the Kennel dataset are shown in Figures 11.c and 11.d. The best F-Score is achieved for the 1500×1500 resolution with $\sigma = 2.5$. The lower optimal σ value can be attributed to the Kennel dataset having images with more rings on the disk, averaging 30 rings. In comparison, the UruDendro one has 19 rings per disk on average. Table 3 summarizes the results of this experiment.

6.3.2 Pith position sensibility

The next experiment assesses the method's sensitivity to errors in the pith estimation. Figure 12.a shows 48 different pith positions used in this experiment (eight different pith positions across six rays). These radially displaced pith positions are selected as follows:

- We define an error step along a ray as 25% of the first ring equivalent diameter.
- Three positions are marked inside ring 1, with errors 25%, 50%, and 75% off the GT center in the ray direction.
- One position is marked on ring 1.

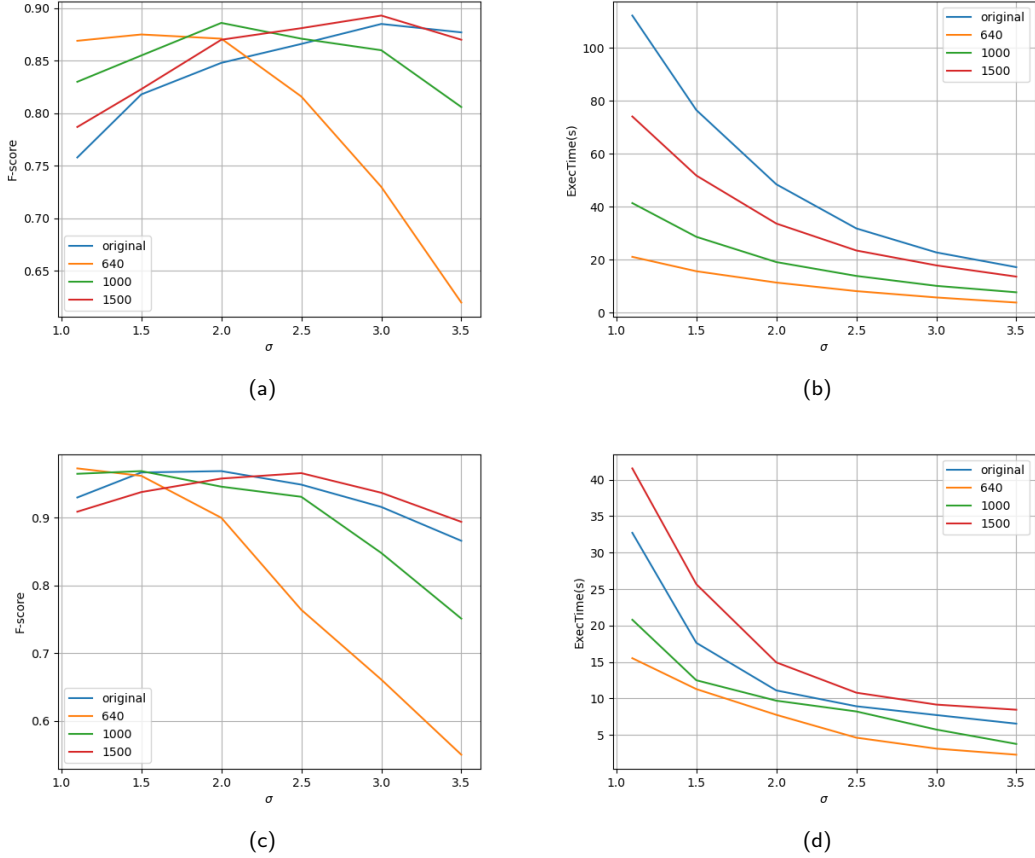


Figure 11: Influence of the image size and edge detector σ parameter experiment. Each curve represents a different image resolution: 640×640 , 1000×1000 , 1500×1500 , and the original resolution (in blue). (a) Average F1 vs. σ for different image sizes over the UruDendro dataset. (b) Average execution time (in seconds) vs σ for different image sizes over the UruDendro dataset. (c) Average F1 vs. σ for different image sizes over the Kennel dataset. (d) Average execution time (in seconds) vs σ for different image sizes over the Kennel dataset.

- Three positions are marked between the first and second rings, with the same increasing errors in the ray direction.
- Finally, another position is marked on ring 2.

We executed the algorithm for each disk and pith position of the UruDendro dataset (size of 1500×1500 and $\sigma = 3.0$), resulting in 48 outcomes. We calculated the average RMSE and F-Score measurements for the six-ray directions for each radially displaced pith position. This produced two eight-coordinate vectors, one for RMSE and one for the F-Score. Figures 12.b and 12.c illustrates the average F-Score and RMSE for each error position across the dataset, respectively. The F-Score decreases as the error in the pith estimation increases, while the RMSE is less sensitive to pith errors.

6.3.3 Metric precision threshold

In this experiment, we examine how performance changes with different values of the th_pre parameter, which determines the number of ring nodes within the influence area to be considered in the detection-to-ground-truth assignation step. Figure 13 displays the results for the UruDendro and Kennel datasets. As anticipated, higher precision leads to lower RMSE but lower F-Score. Based on these findings, we fixed $th_pre = 60\%$ as the default value, which appears to be a good compromise.

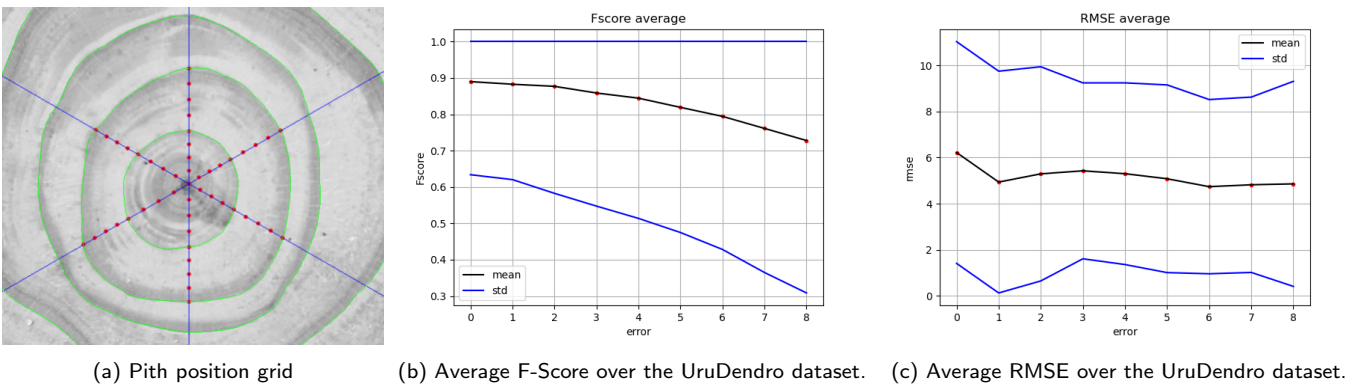


Figure 12: Pith position experiment. (a) Eight different pith positions are marked given six ray directions. We executed the method for each marked pith position. GT rings are in green. (b and c) For each disk of the UruDendro dataset, we run the method using the 48 different pith positions. Results are averaged over the six rays' directions per error position. The X-axis values correspond to increments of 25 % in error, i.e., the value 2 implies an error of 50 % of the first ring equivalent diameter in the pith position concerning the GT.

6.4 Results

This section provides a quantitative analysis of the CS-TRD method performance on challenging images in the datasets. Figure 14 illustrates some results of the CS-TRD over the UruDendro dataset. Note the successful performance of CS-TRD on disks with cracks (F02b), knots (L03c), and fungus (L02b). The mean F-Score for the whole dataset is 0.89 (Table 3), indicating the successful detection of rings in complex images containing knots, fungus, and cracks. Results of the CS-TRD algorithm on other samples of the Urudendro dataset are in the supplemental material.

The upper row of Figure 15 illustrates how the method performs in the presence of knots. The disk F04c fails to detect the first and third rings, identifies a false ring over the knot, and misses the last ring. Despite these errors, the method detected 19 rings, with only one false detection, and missed two rings, resulting in an F1-Score of 90%. The lower row of Figure 15 shows the CS-TRD results for disk L09e. Despite two significant cracks and several fungus stains, the method successfully detects 13 out of 15 rings, with one false detection. As a result, it achieves an F1-Score of 90%.

Some results for the Kennel dataset are shown in Figure 16. The results for the whole dataset can be seen in the supplementary material. The mean F-Score is 0.97 (Table 3). At most, three rings are not detected per disk. In the worst case, one ring is mistakenly detected per image, usually the last one (sometimes incomplete) or the core. In Figure 17, we illustrate the example of disk *AbiesAlba*. The edge parameter is set too high ($\sigma = 2.5$), causing the edge detector to fail to detect the pith. Additionally, the red chain in Figure 17.c is not closed because its size is smaller than 180 degrees (the *information_threshold* parameter is fixed once and for all). However, the method effectively detects the rings over the knot.

6.5 Comparison between CS-TRD and INBD methods.

The only other method with available code for automatically detecting tree rings in wood cross-section images is the Iterative Next Boundary Detection Instance Segmentation (INBD) proposed by Gillert et al. [7]. Note that this method was designed for Microscopy Images of Shrub Cross Sections, which differ from the ones we are working with regarding image resolution and species characteristics. In the INBD method, the image is segmented into the background, ring boundaries, and the pith region. Then, the circular image is transformed into polar coordinates using the pith's center as the origin. Iterative image patches are then extracted, and rings are segmented individually

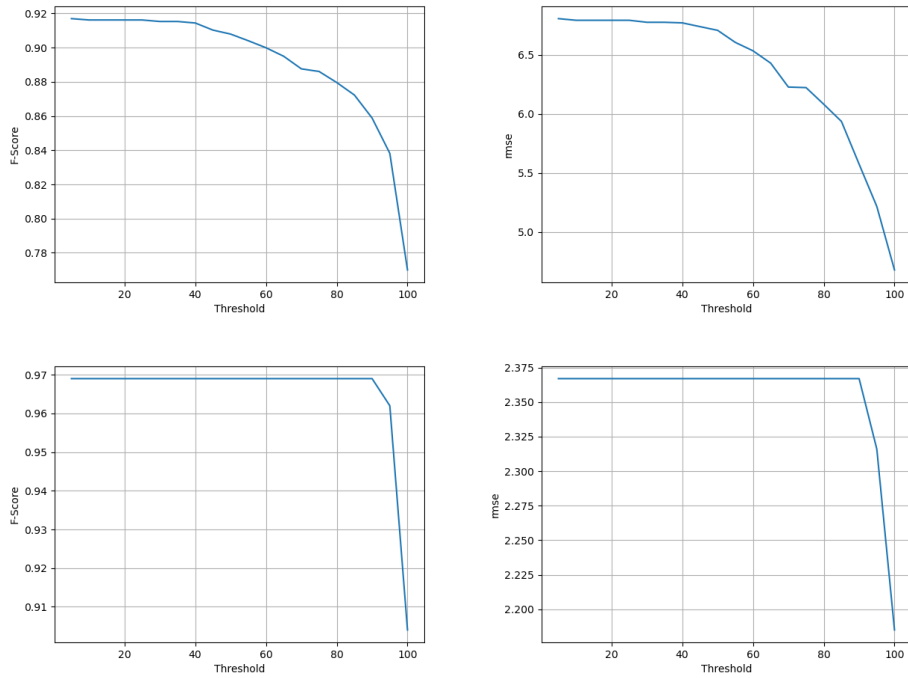


Figure 13: Performance metrics were computed for different values of the th_pre parameter. The first row shows the results for the Urudendro dataset, and the second row for the Kennel dataset. The left column shows the average F-Score, and the right column shows the average RMSE.

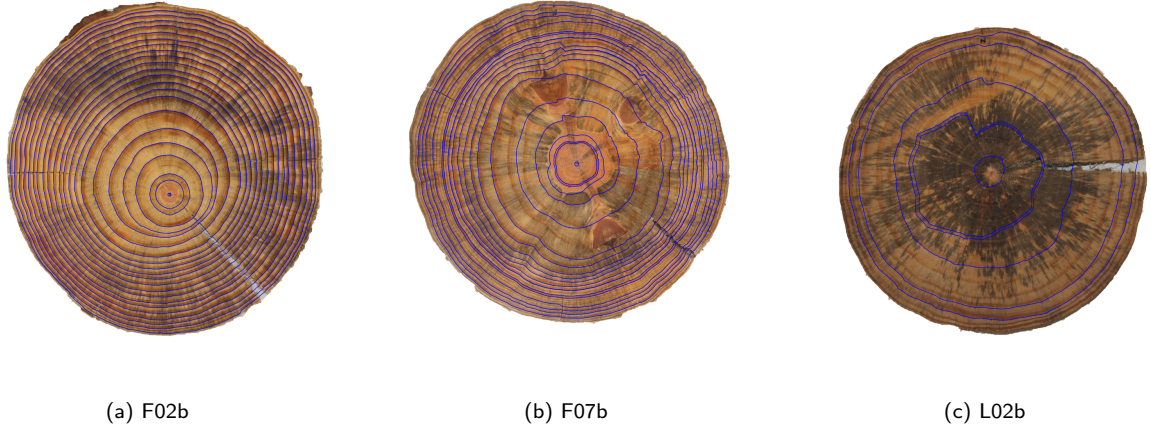


Figure 14: The CS-TRD method predicted detections (shown as blue curves) in some images of the UruDendro dataset.

from the inner to the outer rings. Both stages employ a U-NET network.

Furthermore, the ground truth pith location is used as input in the experiments for the CS-TRD. To ensure a fair comparison, the second stage of the INBD method is modified to take the pith boundary as input.

To train the INBD model with the UruDendro dataset, we randomly divided it into train, validation, and test sets with 40, 12, and 12 images, respectively. Guillert et al. trained their model with the EH dataset, which consists of 82 images with 949 rings. Our UruDendro dataset comprises 64 images and 1123 rings. For training the INBD model, each image is divided into patches determined by successive rings in polar coordinates, ensuring that each patch includes an entire ring. Even though the EH dataset has more images, the UruDendro dataset has more rings per image. Considering the

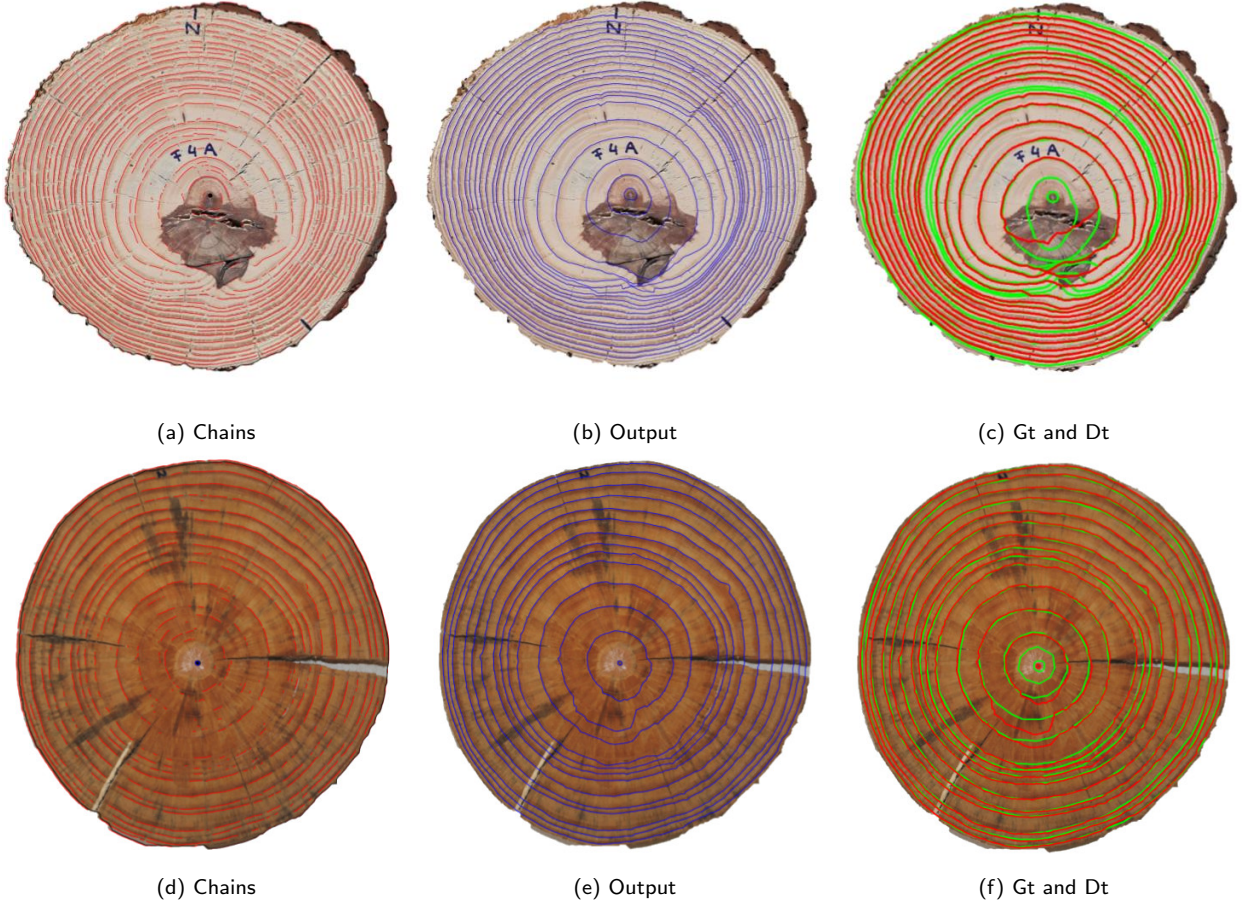


Figure 15: Upper row: CS-TRD result for disk F04c. Note the impact of the knot on the edge detection step. (a) chains, (b) detected rings, (c) GT rings in green, and detected rings in red. Lower row: CS-TRD result for disk L09e. The method successfully detects almost all the rings ($FN=2$ and $FP=0$) despite cracks and fungus stains. (d) chains, (e) detected rings, (f) GT rings in green, and detected rings in red.



Figure 16: CS-TRD results for images from the Kennel dataset with 1500×1500 image size and $\sigma = 2.5$.

total number of tree rings, both datasets are comparable.

The INBD method relies on two important hyperparameters: the number of iterations at each epoch (n) and the image size factor (downsample). We seek the best-performing INBD model by exploring a grid with $n \in \{1, 2, 3, 4\}$ and $downsample \in \{0, 2, 4\}$. The model was trained using the UruDendro training and validation sets. The model that exhibits the best performance on the validation set

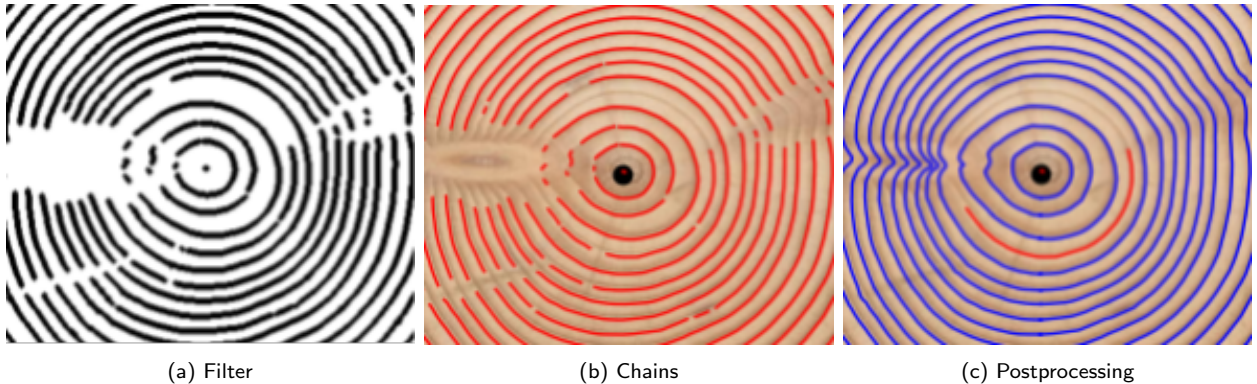


Figure 17: CS-TRD result for *AbiesAlba1* image from the Kennel Dataset (zoom over pith center). a) Filter stage output, b) Chain stage output, c) Postprocessing stage output. In a) and b), we can see that the method fails to detect edges for the pith. The σ threshold may be too high to detect things at this resolution. In c), we can see that the red chain was not closed due to a size smaller than the *information_threshold* value (180)

was chosen. For training, we utilized the ClusterUy infrastructure, as described in ClusterUy [13], equipped with an Nvidia Tesla P100 GPU with 12GB of RAM. The hyperparameters $n = 3$ and $downsample = 0$ yield the best performance on the validation set.

Table 4: Comparative results between INBD and CS-TRD methods over the test set of images from the UruDendro dataset. To compare the execution times the same HW was used. \uparrow (\downarrow) indicates higher (lower) values are better.

| Method | P \uparrow | R \uparrow | F \uparrow | RMSE (pixels) \downarrow | Time CPU (seconds) \downarrow |
|--------|--------------|--------------|--------------|----------------------------|---------------------------------|
| INBD | 0.75 | 0.84 | 0.79 | 5.7 | 7.5 |
| CS-TRD | 0.94 | 0.88 | 0.91 | 3.0 | 18 |

Table 4 compares the performance of both methods using the test set from the UruDendro dataset. When using the same CPU hardware, we observe that the INBD execution time is better, running at an average of 7.5 seconds compared to 18 seconds for CS-TRD. In terms of performance, CS-TRD outperforms the INBD model in precision, recall, and F-score. When considering the RMSE metric, CS-TRD performs slightly better than INBD, with a difference of 2.7 pixels. As a point of reference, the RMSE difference between the human annotators on the UruDendro dataset is around 2.5 pixels.

Figure 18 illustrates a qualitative comparison between both methods for two disks of the UruDendro dataset. Subfigures a, c, e, and g superpose the detected rings in red and the ground truth rings in green, while subfigures b, d, f, and h depict the absolute radial error between the automatic detections and the GT disks. In the upper row, the results for disk F03b are shown. CS-TRD produced 20 True Positives, 1 False Positive, and 3 False Negatives, compared to 19 True Positives, 3 False Positives, and 4 False Negatives for INBD. The INBD method is iterative, and an error produced in a certain ring is propagated to the next rings outward, as seen in subfigure d. This significantly increases the RMSE error (9.2 for the INBD and 1.1 for the CS-TRD). The lower row of Figure 18 illustrates the results for a disk with a high amount of fungus stains (L02b), which produces an important number of false detections (20) by the INBD method.

7 Conclusions and future work

We presented an automatic method for Tree Ring Detection of cross-section wood images. It achieves an F-Score of 97% in the Kennel dataset and 89% in the more complex UruDendro dataset. The CS-TRD method outperforms deep learning state-of-the-art methods such as the INBD [7] in the

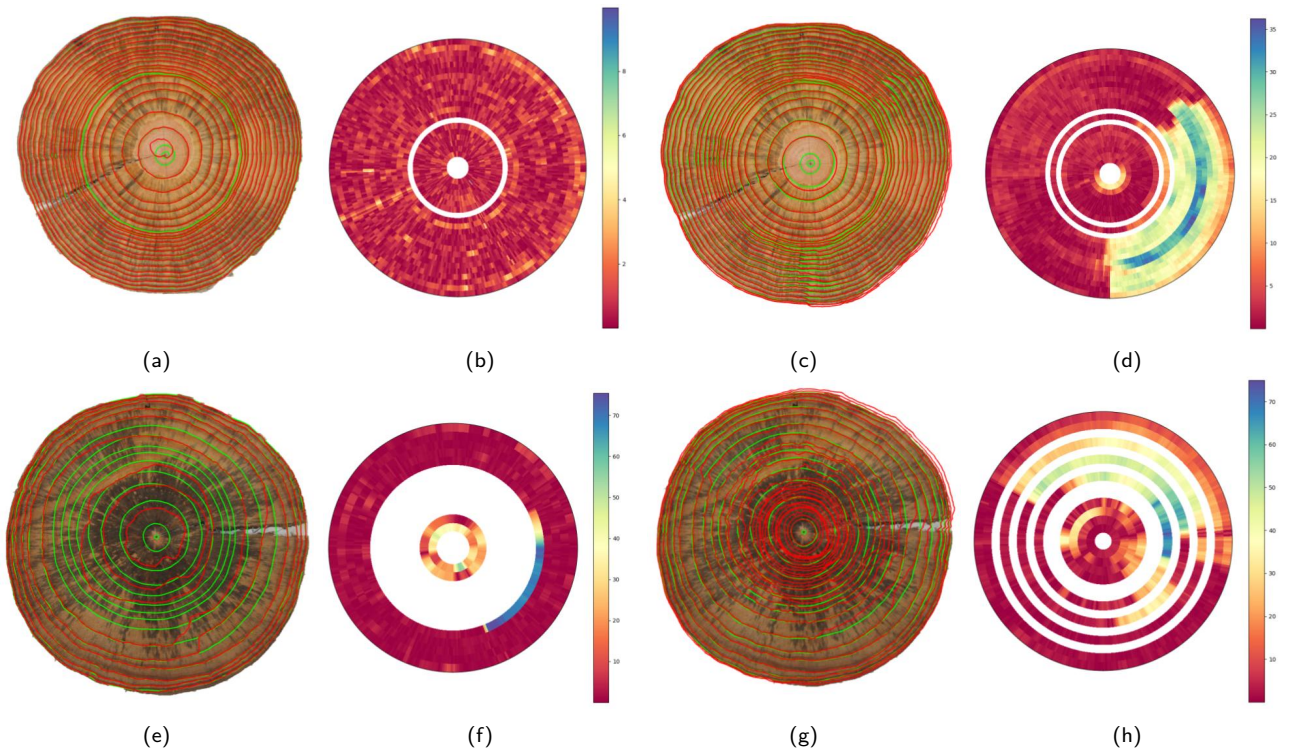


Figure 18: Upper row, results of CS-TRD (left) and INBD (right) methods for disk F03b of UruDendro. In (a) and (c), the ring detections are shown in red, and the GT rings in green. In (b) and (d), the absolute radial error between the ring detections and the GT rings is displayed. (The red indicates a low error, and the blue indicates a high error. A white band indicates no detection for a given ground truth ring. The results of the CS-TRD (left) and INBD (right) methods for disk L02b of UruDendro are shown in the lower row. In (e) and (g), the ring detections are shown in red, and the GT rings in green. In (f) and (h), the absolute radial error between the ring detections and the GT rings is displayed (red indicates a low error, and blue indicates a high error. A white band indicates no detection for a given ground truth ring).

Pinus taeda species. It performs well even in the presence of fungus, cracks, and knots and in two different species (*Abies alba* and *Pinus taeda*).

The method runs at an average execution time of 17 seconds in the UruDendro dataset and 11 seconds in the Kennel dataset on an Intel Core i5 10300H workstation with 16 GB of RAM (without GPU). Compared with the time each annotator needs to manually delineate every disk, 3 hours on average, is a vast improvement. CS-TRD can be fully implemented in C++ to accelerate the execution time compared to the Python implementation². This will allow using the method in real-time applications.

In the future, we plan to include the automatic pith detection, extend the method to other tree species, and explore machine-learning techniques to improve the results.

Image Credits



Images from the UruDendro dataset.



Images taken from a [6]



original images from the Kennel dataset.

²<https://medium.com/agents-and-robots/the-bitter-truth-python-3-11-vs-cython-vs-c-performance-for-simulations-babc85cdfe5>

References

- [1] MAURICIO CERDA, NANCY HITSCHFELD-KAHLER, AND DOMINGO MERY, Robust tree-ring detection, in Advances in Image and Video Technology, Second Pacific Rim Symposium, PSIVT 2007, Santiago, Chile, December 17-19, 2007, Proceedings, Domingo Mery and Luis Rueda, eds., vol. 4872 of Lecture Notes in Computer Science, Springer, 2007, pp. 575–585.
- [2] RÉMI DECELLE, PHUC NGO, ISABELLE DEBLED-RENNESSEN, FRÉDÉRIC MOTHE, AND FLEUR LONGUETAUD, Ant Colony Optimization for Estimating Pith Position on Images of Tree Log Ends, Image Processing On Line, 12 (2022), pp. 558–581. <https://doi.org/10.5201/ipol.2022.338>.
- [3] FRÉDÉRIC DEVERNAY, A non-maxima suppression method for edge detection with sub-pixel accuracy, tech. report, INRIA RESEARCH REP. 2724, SOPHIAANTIPOLIS, 1995.
- [4] PHILIPP DUNCKER, Detection and Grading of Compression Wood, 11 2014, pp. 201–224.
- [5] ANNA FABIJAŃSKA AND MAŁGORZATA DANEK, Deepdendro – a tree rings detector based on a deep convolutional neural network, Computers and Electronics in Agriculture, 150 (2018), pp. 353–363.
- [6] ANNA FABIJAŃSKA, MAŁGORZATA DANEK, JOANNA BARNIAK, AND ADAM PIÓRKOWSKI, Towards automatic tree rings detection in images of scanned wood samples, Computers and Electronics in Agriculture, 140 (2017), pp. 279–289.
- [7] ALEXANDER GILLERT, GIULIA RESENTE, ALBA ANADON-ROSELL, MARTIN WILMING, AND UWE FREIHERR VON LUKAS, Iterative next boundary detection for instance segmentation of tree rings in microscopy images of shrub cross sections, 2022.
- [8] RAFAEL GROMPONE VON GIOI AND GREGORY RANDALL, A sub-pixel edge detector: an implementation of the canny/devernay algorithm, Image Processing On Line, 7 (2017), pp. 347–372. <https://doi.org/10.5201/ipol.2017.216>.
- [9] MICHAEL HENKE AND BRANISLAV SLOBODA, Semiautomatic tree ring segmentation using active contours and an optimised gradient operator, Forestry Journal, 60 (2014), pp. 185 – 190.
- [10] POL KENNEL, PHILIPPE BORIANNE, AND GÉRARD SUBSOL, An automated method for tree-ring delineation based on active contours guided by DT-CWT complex coefficients in photographic images: Application to abies alba wood slice images, Comput. Electron. Agric., 118 (2015), pp. 204–214.
- [11] KAYLA MAKELA, TIM OPHELDERS, MICHELLE QUIGLEY, ELIZABETH MUNCH, DANIEL CHITWOOD, AND ASIA DOWTIN, Automatic tree ring detection using jacobi sets, 2020.
- [12] HENRY MARICHAL, DIEGO PASSARELLA, CHRISTINE LUCAS, LUDMILA PROFUMO, VERONICA CASARAVILLA, MARIA NOEL ROCHA GALLI, SERRANA AMBITE, AND GREGORY RANDALL, UruDendro: An Uruguayan Disk Wood Database For Image Processing. <https://iee.fing.edu.uy/proyectos/madera>.
- [13] SERGIO NESMACHNOW AND SANTIAGO ITURRIAGA, Cluster-uy: Collaborative scientific high performance computing in uruguay, in Supercomputing, Moisés Torres and Jaime Klapp, eds., Cham, 2019, Springer International Publishing, pp. 188–202.
- [14] KRISTIN NORELL, JOAKIM LINDBLAD, AND STINA SVENSSON, Grey weighted polar distance transform for outlining circular and approximately circular objects, 14th International Conference on Image Analysis and Processing (ICIAP 2007), (2007), pp. 647–652.
- [15] MIROSLAV POLÁEK, ALEXIS H. ARIZPE, PATRICK HÜTHER, LISA WEIDLICH, SONJA STEINDL, AND KELLY L. SWARTS, Automation of tree-ring detection and measurements using deep learning, bioRxiv, (2022).

- [16] XUEBIN QIN, ZICHEN ZHANG, CHENYANG HUANG, MASOOD DEHGHAN, OSMAR R. ZAÏANE, AND MARTIN JÄGERSAND, U²-net: Going deeper with nested u-structure for salient object detection, CoRR, abs/2005.09007 (2020).
- [17] KENTARO WADA, Labelme: Image Polygonal Annotation with Python.
- [18] HONG ZHOU, RONG FENG, HUA HONG HUANG, ER PEI LIN, AND JUN LIN YU, Method of tree-ring image analysis for dendrochronology, Optical Engineering, 51 (2012), p. 077202.